# Geophysical signature of two contrasting Andean rock glaciers.

Giulia de Pasquale[1], Rémi Valois[2], Nicole Schaffer[1], and Shelley MacDonell[1]

[1]Centro de Estudios Avanzados en Zonas Áridas – CEAZA, Raúl Bitrán 1305, La Serena, Chile

[2]Environnement Méditerranéen et Modélisation des Agro-Hydrosystèmes, Université de Avignon - EMMAH, Domaine Saint-Paul, Site Agroparc 228, Avignon, France

**Correspondence:** Giulia de Pasquale (giulia.depasquale@ceaza.cl)

**Abstract.** In semi-arid Chile, rock glaciers cover a surface area that is estimated to be approximately four times larger than that occupied by glaciers. Understanding their role in freshwater production, transfer and storage is likely of primary importance, especially in this area of increasing human pressure on water resources and high rainfall variability. To understand their current and future hydrological role it is necessary to characterize their internal structure (e.g., internal boundaries, ice, air, water and rock content). In this paper, we present the results and interpretations of electrical resistivity and refraction seismic tomography profiles on two contrasting rock glaciers in the Chilean Andes. These are the first in situ measurements in Estero Derecho: a natural reserve at the headwaters of the Elqui River, where these two rock glaciers are located. Our measurements confirm that El Ternero (intact rock glacier) contains significant reserves of ice while El Jote contains little to no ice (relict rock glacier). Within our study, we highlight the strong differences in the geophysical responses between intact and relict rock glaciers and propose a diagnostic model that differentiates between intact and relict rock glaciers.

## 1 Introduction

High mountain environments are delicate geosystems under increasing human pressure and represent important geoecological indicators of a changing climate of the areas where they are situated (Hock et al., 2019). In particular, in semi-arid Chile (between 29°and 34°S), rock glaciers cover a surface area that is approximately four times larger than that occupied by glaciers (Azòcar and Brenning, 2010) and may play an important role in the hydrological cycle (Harrington et al., 2018; Schaffer et al., 2019; Halla et al., 2020). While the former statement is based on a publication from 2010, more recent studies (Bodin et al., 2010; Barcaza et al., 2017) have confirmed that the areal extent of rock glaciers in the semi-arid Andes has remained unchanged, so we infer that this statement is still valid today. While melt from seasonal snow cover provides a greater contribution to annual streamflow than rock glaciers, the snow cover only lasts 1 to 2 months after the last winter snowfall (Favier et al., 2009), so glaciers, rock-glaciers and other surface ice bodies are the main water source when river levels are at a minimum, especially during dry years (Gascoin et al., 2011). A recent study quantifying the contribution of rock glaciers to streamflow in the La Laguna Catchment (Elqui Province) indicated that the contribution at the end of summer may be significant (Schaffer et al., 2019), although their estimated contribution was based on preliminary data and needs to be refined.

Rock glaciers are typically lobate or tongue-shaped landforms composed of rock fragments, sediment, ice, often unfrozen pore water, and contain air filled pore spaces and cavities (Barsch, 1996; Cogley et al., 2011; Hauck et al., 2011). They are the visible expression of the deformation of ice-rich creeping mountain permafrost and can act as climate change indicators in high mountain environments (Barsch, 1989; Bodin et al., 2010; Berthling, 2011). Rock glaciers can be classified according to the speed at which they move down slope through the deformation of subsurface ice and or ice-rich sediments (Ballantyne, 2002). Active rock glaciers contain enough ground ice to induce internal deformation and movement downslope (e.g. decimeter to meters per year; Delaloye and T, 2020) most often identified by geomorphological evidence (e.g. steep frontal slope), whereas inactive rock glaciers contain less ice and are essentially stagnant (Barsch, 1996; Brenning et al., 2007; Schaffer et al., 2019). Both active and inactive rock glaciers are categorized as intact, meaning that they contain ice. Conversely, relict rock glaciers contain little to no ice (Barsch, 1992; Jones et al., 2018). Because of their debris cover, rock glaciers are generally more resilient to climate (atmospheric) changes (Jones et al., 2018; Harrington et al., 2018), although there are indirect measurements (e.g. a significant increase in solute concentrations for rock glacier-fed lakes, increased velocities) which suggest that rock glaciers in the European Alps have experienced increased melt rates in recent decades (Krainer and Mostler, 2006; Thies et al., 2007).

Studies on Andean rock glaciers (Schrott, 1996; Croce and Milana, 2002; Schaffer et al., 2019) indicate that they store significant amounts of water and emphasize their role in freshwater production, transfer and storage. A study of the Tapado Glacier complex, composed of a debris-free glacier, debris-covered glacier and a rock glacier in the Elqui watershed of the Chilean Andes (Pourrier et al., 2014), describes the contrasting hydrological output of each formation. While water from the debris-free glacier was highly correlated with daily and monthly fluctuations in temperature and solar radiation, the glacier foreland (composed of the debris-covered glacier, rock glacier, and moraines) buffered this variability acting as a reservoir during high melt periods and supplying water downstream during low melt periods. This slow, diffuse transfer of water was attributed to a highly capacitive but weakly transmissive medium composed of a heterogeneous mixture of ice and rock debris. Harrington et al. (2018) investigated the impact of an inactive rock glacier in Canadian Rockies to the basin stream-flow. At this site, the rock glacier surface layer is composed of coarse blocky sediments that allow the rapid infiltration of snow-melt and rain water which accumulates within the rock glacier. Discharge from the rock glacier is slower than from the surrounding landscape and this rock glacier is therefore able to provide up to 100 % of the basin streamflow during summer base-flow periods despite the fact that it drains less than 20 % of the watershed area. A study on a relict rock glacier in Austria (Winkler et al., 2016), showed that this rock glacier type can act as an aquifer delaying the release of spring runoff by up to several months. These studies suggest that rock glaciers may play an important role in moderating discharge to ensure sufficient water reserves exist when water levels are at a minimum. However more studies are urgently needed to better understand their hydrological role in semi-arid Chile, where highly variable rainfall and little to no precipitation during the warmest months of the year (Garreaud, 2009; Valois et al., 2020a), result in water scarcity especially at the end of summer (Oyarzùn and Oyarzùn, 2011).

The water reserve available within rock glaciers (as a frozen and/or liquid state) is particularly valuable within the context of a warming climate. To estimate the volume a rock glacier occupies, it is crucial to know its geometry, to identify the bottom of the rock glacier (bedrock geometry) and the bottom of the active layer (depth to permafrost). In addition, since only part of the rock glacier is composed of ground ice, the percentage of ice must be quantified. This can vary considerably, normally ranging from 40 % to 70 % in active rock glaciers (Barsch, 1996; Monnier and Kinnard, 2015).

Rock glacier composition can be derived from direct observations (e.g., boreholes logs, outcrops, tunnels and temperature measurements), borehole and surface-based geophysical observations (Hausmann et al., 2007). Surface-based geophysical methods represent an economic approach to investigate the physical structure and properties of the Earth's subsurface. These methods ability to provide information over large areas with relative high resolution and in a non invasive manner makes them a useful tool for studying ground ice and permafrost in high mountain environments, where difficult site access limits the possibility of deep borehole drilling (Maurer and Hauck, 2007; Hauck and Kneisel, 2008). For these reasons, geophysical methods have been used extensively to investigate the internal structure of rock glaciers (Hauck and Kneisel, 2008) and other geoforms such as high altitude wetlands (Valois et al., 2020b). Among the different techniques, the most implemented include refraction seismic tomography (RST), electrical resistivity tomography (ERT), ground-penetrating radar (GPR) and gravimetry (Langston et al., 2011; Maurer and Hauck, 2007; Colucci et al., 2019; Pourrier et al., 2014).

In this paper, we characterize an intact (El Ternero) and stagnant (El Jote) rock glacier located in the Chilean Andes. On both rock glaciers we conducted coincident RST and ERT profiles that we interpret both separately and jointly through the petrophysical four phase inversion scheme by Wagner et al. (2019). The geophysical profiles collected are the first in situ measurements over rock glaciers in the reserve (Estero Derecho) where the two formations are located. Through the analysis of the inversion model results, we were able to underline the response differences of the geophysical methods between El Ternero and El Jote rock-glaciers and to infer key information regarding the subsurface structure and composition of the two formations. This is the first study we are aware of that compares the geophysical signature of intact versus stagnant rock glaciers using multiple geophysical methods.

## 2 Study Area

The study area is in north-central Chile ($\sim 30°$ S) where there is a sharp altitudinal gradient between the Pacific Ocean and the Andes mountains with peaks rising above 6000 m a.s.l. less than 150 km east of the ocean. At this latitude there exists intensive compression between the Nazca and South American tectonic plates, associated with a flat slab segment, which has resulted in the creation of major transverse valleys (Yáñez et al., 2001) such as the Elqui Valley in the Coquimbo Region (Fig. 1a). The floor and marginal terraces of the Elqui Valley are of Quaternary alluvium. Surrounding mountains are steep and mostly intrusive with some volcanic, volcano-sedimentary, and metamorphic rocks Paleozoic-Triassic in age (Aguilar et al., 2013; Valois et al., 2020a). Rock glaciers and periglacial landforms are numerous, particularly above 4000 m a.s.l.(Dirección General de Aguas (DGA) glacier inventory, 2012, unpublished data)

The study site is within the semiarid Andes of Chile at the southern edge of the Arid Diagonal and Atacama Desert (Sinclair and MacDonell, 2016). Specifically it is located at the headwaters of the Elqui River within the Coquimbo Region in a nature reserve called Estero Derecho (Fig. 1b). In the city of La Serena on the coast the annual precipitation is $\sim 90\ \mathrm{mm\ a^{-1}}$ (average from 1981-2016; Valois et al., 2020b), drastically lower than the average annual precipitation for Chile of $\sim 1525\ \mathrm{mm\ a^{-1}}$ (DGA., 2016). At the same time, demand from the agricultural sector, mining industry, and municipal water supply are high and water allocation has already been exhausted (DGA., 2016). Precipitation increases with elevation reaching $\sim 160\ \mathrm{mm\ a^{-1}}$

at 2900 m a.s.l. in the Estero Derecho valley (Valois et al., 2020b). Increased precipitation at higher altitudes allows for the formation of a seasonal snow pack that completely melts during the spring and summer seasons (Réveillet et al., 2020). Variability in precipitation at an inter-annual time scale is linked to El Niño Southern Oscillation (ENSO; Favier et al., 2009), while at a decadal time scale it is linked to the Pacific Decadal Oscillation (Núñez et al., 2013). Precipitation has decreased since 1870 by $\sim 0.52\,\mathrm{mm\,a^{-1}}$ at La Serena. The mean annual air temperature at a station at 3020 m a.s.l. within Estero Derecho was 6.7°C between 2016-2020.

Within the nature reserve there are no debris-free glaciers, only rock glaciers and other periglacial landforms such as protalus ramparts and gelifluction lobes. The two rock glaciers measured in this study are locally known as "El Jote" and "El Ternero" and are in the eastern part of the nature reserve (Fig. 1b) at 3700-3870 m a.s.l. and 4170-4510 m a.s.l., respectively. El Ternero is the largest intact rock glacier within Estero Derecho, has a lobate shape and clear flow features such as ridges and furrows, a steep frontal talus slope ($\sim 40°$), and well defined lateral margins. There are a number of depressions $\sim 5\,\mathrm{m}$ deep on the surface and a pond on the surface covering an area of $\sim 80\,\mathrm{m}^2$. We interpret these depressions as thermokarst degradation features. El Ternero is 1.93 km long, has a maximum width of 0.51 km, and an area of 0.60 $\mathrm{km}^2$. It is moving at a rate of $\sim 1\,\mathrm{ma}^{-1}$ and lowering by $\sim 0.2\,\mathrm{ma}^{-1}$ (based on three repeat differential GPS measurements taken in the summer of 2018-2019 and 2019-2020 between 4206 - 4417 m elevation). In contrast, El Jote has poorly defined flow features and a moderately steep frontal slope ($\sim 24°$). This landform is stagnant according to unpublished repeat differential GPS measurements taken taken at five locations in the summer of 2018-2019 and 2019-2020. The lack of obvious flow features and its location within a cirque basin point toward the same conclusion. El Jote is 0.86 km long, has a maximum width of 0.48 km, and covers $0.31\,\mathrm{km}^2$. Its surface is characterized by lobes as well as signs of subsidence such as depressions.

At El Ternero a stream passes adjacent to the former and eroded terminal moraine of the glacier. The waterway initiates on the mountain slope above and south of the glacier and continues down-slope, eventually feeding a high altitude wetland and the main waterway within the reserve, Estero Derecho. There is no evidence of water at the surface directly below the current frontal slope of the rock glacier. However, a substantial amount of water can be heard running below the rock glacier surface within topographic depressions on the surface. At El Jote water emerges $\sim 200\,\mathrm{m}$ east of the main landform in a topographic low at $\sim 3740$ m a.s.l. It is unclear if this water originates from the rock glacier, another periglacial landform, or a groundwater source. There is a small periglacial feature directly above that may be contributing, but no other obvious source of water visible at the surface. The waterway continues for $\sim 600$ m where it disappears $\sim 100$ m below the frontal slope of the rock glacier. Water emerges in another, larger depression, along the same flow path $\sim 550$ m below the front of the rock glacier and continues down-slope, contributing to an alpine wetland (i.e. bofedal) and Estero Derecho. There is vegetation adjacent to the water; in contrast there is little to no vegetation in the surrounding landscape.

## 3 Theory and Methods

### 3.1 Geophysical measurements

Surface-based geophysical methods provide information about subsurface physical properties and have been extensively used to investigate the internal structure of rock glaciers (Hauck and Kneisel, 2008). In particular, electrical resistivity and seismic refraction tomography are common choices for the characterization of rock glacier internal structure, even though their employment in mountainous environments demands specialised techniques for sensor coupling, data acquisition and inversion routines.

#### 3.1.1 Electrical Resistivity Tomography (ERT)

ERT aims to estimate the subsurface electrical resistivity ($\rho$) by injecting direct electric currents (DC) into the ground and measuring electric voltages at different locations. Data are obtained using a large number of resistance measurements made from spatially-distributed four-point electrode configurations (Binley and Kemna, 2005). The geometry of the current injection and potential electrode pairs are varied with typical set-ups involving many tens of electrodes and several hundred or thousand data-points. These data are then inverted to infer the spatial distribution of electrical resistivity in the subsurface (Dahlin, 1996).

Electrical resistivity quantifies the current density flowing through a cross-sectional area along a given length. In most rocks and soils, electrical current is carried by movements of ions in the pore water (electrolyte conduction) and by the movement of mobile ions in an electrical diffuse layer above the mineral surface (surface conduction - Revil and Glover, 1997), with the actual mineral matrix practically acting as an insulator (Lesmes and Friedman, 2005). Due to the high contrast in resistivity between saturated and unsaturated sediments, and the marked increase of resistivity values at the freezing point, resistivity techniques have been useful in both hydrology (de Lima, 1995; Daily et al., 1992; Valois et al., 2018b, a) and permafrost-characterization studies (Evin et al., 1997; Hauck et al., 2003; Langston et al., 2011). In periglacial environments, the use of ERT is particularly popular due to the contrasting electrical resistivity corresponding to lithological media, water (highly conductive) and ice (which is assumed to be an electrical insulator). In Table 1 we list the relevant values for electrical resistivity in rock glacier environments, compiled from the literature.

The main limitation for ERT is the need for the electrodes to have a good galvanic contact with the ground. Its application within the surveys was therefore problematic due to the extremely high contact electrical resistivity caused by air pockets between the electrodes and the ground surface. Following the methodology of Maurer and Hauck (2007), we attenuated this problem by both facilitating the injection of electric current into the ground by attaching sponges soaked in salt water to the electrodes, and in addition, increasing the measured voltage by implementing the Wenner-Schlumberger array configuration (its low geometrical factor provides larger measured voltages compared to other options).

### 3.1.2 Refraction Seismic Tomography (RST)

RST is based on the analysis of first arrival traveltimes of critically refracted seismic waves to reconstruct seismic P-wave (i.e., compressional wave) velocity models (Nolet, 1987; White, 1989). When seismic waves impinge on velocity boundaries, they change their direction of propagation. At a critical angle that depends on the velocity contrast, head waves are created that move along the interface at the speed of the faster lower-lying layer velocity and refracted waves are emitted. These refracted waves are measured by the receiver and the timing of their arrival (i.e., first-arrival travel times) are the main observations used in seismic refraction surveys.

Seismic velocity is the rate at which seismic waves propagate through rocks and soils and this generally increases with material density. In periglacial environments the large range of observed velocity values (Table 1) is favourable for the application of RST, due to the different values expected for lithology and frozen materials. For this reason seismic refraction has been successfully used on rock glaciers since the 1970s (Barsch, 1971; Potter, 1972). In the last two decades the method has been extensively utilized in permafrost studies (Vonder-Mühll et al., 2002; Hauck et al., 2004; Draebing and Krautblatter, 2012) and to monitor hydrodynamic variation impacts on velocities (Valois et al., 2016).

One limitation of first-arrival refraction methods is that they only use a small portion of the information contained in the seismic traces and strongly depend upon the assumption that velocity increases with depth. In the case of velocity inversion (i.e., the deeper medium presenting a lower P-wave velocity than the overlaying one), the refracted wave will bend towards the normal. This gives rise to the so-called “hidden layer" phenomenon (Banerjee and Gupta, 1975). Moreover, surface conditions on rock glaciers highly attenuate seismic energy and make it difficult to couple geophones and seismic sources to the ground. During the collection of seismic data, we were able to partially improve the coupling through the use of a few geophones fastened to metal plates. We also increased the signal-to-noise-ratio by repeating and stacking the same source position multiple times.

## 3.2 Acquisition strategy

Field data collection was conducted during the austral Summer between the end of January and the beginning of February, 2020. The location of sensors and sources of all the profiles were taken with a Trimble differential GPS. At both sites, we acquired the ERT surveys using Syscal Junior switch-48 (IRIS instrument, France) with 48 electrodes spaced 5 m apart and a Wenner-Schlumberger configuration with 23 levels at its maximum; the dipole lengths for the current measurements where of 5, 25 and 45 m, while for the potential measurements where between 15 and 235 m with intervals of 10 m. For the El Jote rock glacier, the profiles length was 690 m (Fig. 2a and b), obtained using five sequential roll-alongs in which 50 % of the electrodes stayed in place each time and the other 50 % were displaced along the profile line (Fig. 2e). In total we implemented 144 different electrode positions and obtained 2135 measurement points. For El Ternero the profile length was 575 m (Fig. 2c and d), which was obtained with four sequential roll-alongs. Here we used 120 different electrode positions and obtained 1479 measurement points. We recorded the refraction seismic surveys on both rock glaciers implementing a Geode Exploration Seismograph device (Geometric, USA) along the same lines as for the ERT profiles. The seismic source was a sledge hammer of 15 kg striking on a steel plate and we repeated each shot position (stacking) five times in order to improve the signal-to-noise ratio. For the profile taken on El Jote, we used 48 geophones with a spacing of 5 m and shots in between geophone positions, but spaced 10 m apart. To obtain the length of 690 m we applied five sequential roll-alongs as done for the resistivity line. In the case of El Ternero, the same spacing and configuration was used for both shots and geophones, but after the first line, the failure of one of the cables reduced the number of geophones to 24. The total length of 575 m was then obtained by moving the 24-channels set-up four times and adding off-line shots (Fig. 2f) to link the different acquisitions at distances of 5, 15 and 25 m from the last geophone at each end of the cable. While the geophysical line extended a bit past the edge of the El Jote rock glacier, it was impossible to do so in the El Ternero because of the high slopes of rock glacier edges, making the access too dangerous. Collection of the profiles on El Ternero were logistically more complicated than on El Jote, due to higher altitudes, to the extremely heterogeneous, rocky surface and especially to the failure of one of the geophone cables. The overall data quality for this rock glacier is much lower than for El Jote (Figs. 4a, b and 6a, b). There are less data points since measurements were not conducted for areas with high contact resistance in the case of ERT (almost 1.5 times less than for El Jote) and many traces were too noisy to identify the first arrival traveltimes for RST (more than 3 times less than for El Jote). For both profiles, we manually picked the first arrival travel times on each trace resulting in 4575 picks for El Jote and 1400 for El Ternero. For the ERT observations, the error models resulted in 1.2 % relative error for El Jote and 11.4 % error for El Ternero, which was obtained from the average of the standard deviation for measured apparent resistivities. For the RST, an absolute error of 0.001 seconds was considered, estimated from the average variability of the first arrival picking. The acquisition settings are summarised in Table 2.

### 3.3 Data processing and Inversion

The ERT observation were automatically filtered by the acquisition software which did not take measurements when the contact resistance was too high, while for the seismic refraction traveltime, we manually picked the first arrivals after applying a gain to the seismic traces and therefore the traces were filtered according to our ability of identify the first arrival times.

The inversion algorithms we use in order to interpret the geophysical observations are part of pyGIMLI, an open-source library developed in python for geophysical inversion and modelling (Rücker et al., 2017). On each rock glacier we implement the same discretization mesh for both ERT and RST inversion routines and use a regularization weight of $\lambda = 10$ for the inversion of all the dataset, chosen according to the L-curve analysis (Hansen, 2001). A schematic plot of the L-curve analysis for each dataset collected is given in Figure 3, in all cases we present the model solution L2-norm against the residual L2-norm obtained for $\lambda = 1$, 5, 10, 15, 50 and 100. For both rock glaciers we use an homogeneous resistivity starting model, with a value equal to the median of the apparent resistivities ($\rho_{\mathrm{a}}^{\mathrm{median}} = 4561\ \Omega\,\mathrm{m}$ for El Jote and $\rho_{\mathrm{a}}^{\mathrm{median}} = 36054\ \Omega\,\mathrm{m}$ for El Ternero) and a gradient model for the seismic velocity, starting with 300 $\mathrm{m\,s^{-1}}$ at the top of the tomogram and gradually increasing to 5000 $\mathrm{m\,s^{-1}}$ at the bottom of it. In each case, we refer to the error-weighted chi-square fit, where $\chi^2 = 1$ signifies a perfect fit (Günther et al., 2006), to quantify the resulting model parameters' ability to explain the field observations.

In addition, to quantify the volumetric percentage of water, ice, air and rock within each of the two rock glacier, we implemented the four phase petrophysical joint inversion scheme presented by Wagner et al. (2019) and tested in Mollaret et al.

(2020). For this inversion scheme we kept the same discretization meshes used for the individual inversions. The methodological details regarding this inversion algorithm and its application for this case study are given in Appendix A.

## 4 Results

### 4.1 El Jote

Figure 4 displays the (a) refraction seismic and (b) electrical resistivity datasets collected on El Jote rock glacier, together with the velocity (c) and resistivity (d) tomograms obtained from their individual inversion. After 15 iterations we obtain an $\chi^2$ of 1.43 for the ERT and 1.38 for the traveltime data. At the top of the parameter domain the model results show low velocity ($\mathrm{v} < 10^3\ \mathrm{m\,s^{-1}}$) and high resistivity ($\rho > 10^4\ \Omega\ \mathrm{m}$), notably at approximately 300 m along the profile line, where the bulk of high resistivity values are concentrated and velocities are at a minimum. We interpret this layer as unconsolidated to highly fractured rocks with air filling pore spaces. This is consistent with field observations, where boulders are visible at the surface and possibly extend downwards along with unconsolidated rock till to depths of 10 to 50 m. At the bottom of the tomogram the velocity model presents high velocity values between 150 m and 250 m (between 50 and 80 m depth) and at approximately 550 m (between 40 and 50 m depth) along the profile line. In the first case the resistivity values are relatively low ($\rho \sim 10^3\ \Omega\ \mathrm{m}$) while at around 500 m they increase one order of magnitude ($\rho \sim 10^4\ \Omega\ \mathrm{m}$). This increase can be explained by a decrease in the pore space, where subsurface material between 150 m and 250 m is in liquid form (low resistivity) while near 550 m it is partly frozen (high resistivity) or by changes in the surface conductivity at the grain/water or ice/water interface (Duvillard et al., 2018).

The results from the petrophysical joint inversion scheme are presented in Figure 5. These confirm the interpretation given for the individual inversion model and complement these results with quantification of the volumetric content of the different subsurface components. The top layer (with a thickness varying between 10 to 50 m along the profile) is mostly air (up to 63 %, see Fig. 5e) with a low rock fraction (with a minimum of 27 % at the surface, see Fig. 5f). Underneath, the unconsolidated rocks are characterized by a decrease in porosity and relatively high content in water (up to 29 %, see Fig. 5c) except near the profile length of 550 m, where the ice content slightly increases to 3 % (Fig. 5d). In addition, the high rock content at the bottom of the domain (88 %, see Fig. 5f) likely represents the top of the bedrock. Besides the similarity in the structure and component interpretation of the subsurface, the transformed velocity and resistivity models (Fig. 5a and b) present differences if compared to the individual inversion results, with overall lower velocity values and higher contrasts in the resistivities.

### 4.2 El Ternero

Figure 6 displays the (a) refraction seismic and (b) electrical resistivity datasets collected on El Ternero rock glacier, together with the velocity (c) and resistivity (d) tomograms obtained from their inversion. After 15 iterations we obtain A $\chi^2$ of 2.1 for the ERT and 0.93 for the traveltime data. The results show a thin layer (approximately 5 m thick) of low velocity and high resistivity which, as for El Jote, reflects the field observations, where boulders are visible at the surface of the rock glacier:

unconsolidated rock with air-filled pore space. Below this layer, P-waves velocity increases gradually for the first 15-20 m up to $\mathrm{v} \sim 3000~\mathrm{m\,s^{-1}}$ and has a sharp increase from 25 m depth ($\mathrm{v} > 4000~\mathrm{m\,s^{-1}}$). We interpret the gradual increase of velocity as a lowering in the pore space, and sharp changes with either the presence of intact rock (i.e., top of the bedrock) or with a significant increase in the amount of ground ice. Also, at approximately 150 m and 450 m of the profile length the resistivity has two low-value anomalies which most likely reflect the presence of water within the pore space.

In Fig. 7 we show the joint inversion results obtained through petrophysical coupling. These results help to clarify the information gained through the comparison of the two individual inversion model results. Indeed, they confirm the presence of a thin top layer (approximately 5 m thick) with moderately high fraction of air (up to 28 %, see Fig. 7e) overlaying a layer with a high ice content (more than 30 % for the majority of the model domain and up to 44 % at its highest concentration (Fig. 7d) except near profile length 150 m and 450 m, where the fraction of water slightly increases to 15 % and 17 %, respectively (Fig. 7c). As in the previous case, the transformed velocity and resistivity models (Fig. 7a and b) present differences if compared to the individual inversion, with overall lower velocity values and higher resistivity values and contrasts.

## 5 Discussion

### 5.1 Data quality and comparison of the inversion routines

For both field sites the acquisition of data and their quality were limited by the environment: the presence of large boulders with air-filled voids between them at the surface of both glaciers attenuated both mechanical and electrical energy propagation. The quality of the data was especially affected in the case of El Ternero rock glacier, which is clearly demonstrated when comparing Figures 4(a)-(b) and 6(a)-(b). It must be stressed that the parameter domains shown in the individual P-wave velocity inversion results and in the petrophysical joint inversion results (Figs. 4c, 6c, 5 and 7) are geometrically delimited by the lowermost ray path but the ray-coverage within the displayed area is limited.

The overall structure of the inversion model results are largely consistent with the main patterns of high/low resistivities and high/low velocities presented in the individual inversion results preserved in the petrophysical joint inversion schemes. Nevertheless, assessment of the numerical values of velocity and resistivity reveal some unrealistic results and differences between the two approaches. In the case of individual inversion results, P-wave velocity models (Figs. 4c and 6c) present some unrealistic values as extremely low velocity at the surface for El Jote ( $\mathrm{v_{min}} \sim 10~\mathrm{m\,s^{-1}}$ ) and extremely high velocity at the bottom of El Ternero ($\mathrm{v_{max}} \sim 10^4~\mathrm{m\,s^{-1}}$). In the first case, the low values are compensated by a high velocity anomaly at the bottom of the model which occupies a larger volume if compared with the results of the joint inversion routine (Fig. 5a), while for El Ternero, the high values are counterbalanced by lower velocity at the surface ($\mathrm{v_{min}} \sim 100~\mathrm{m\,s^{-1}}$) if compared with the one obtained through joint inversion routines ($\mathrm{v_{min}} \sim 900~\mathrm{m\,s^{-1}}$). Also, for both cases the petrophysical joint inversion results present the smaller ranges of P-wave velocities and the smoothest contrasts within the model, which is a consequence of the constraints in the parameters from the petrophysical model and of the simple smooth-constraint scheme implemented. In contrast, for the resistivity inversion model results the petrophysical coupling gives the highest values and sharpest contrasts within the model (Figs. 5b and 7b).

### 5.2 El Jote (stagnant rock glacier)

For El Jote, the results show a top layer (laterally variable between 10 to 50 m thick) of unconsolidated rock with air-filled pore space, especially from 300 m to the end of the profile line. This overlays a layer where the pore space decreases and appears saturated with water for the majority of the line, apart from near 550 m, where the fraction of ice slightly increases to 3 % (Fig.5d). The increased velocity and resistivity at 550 m could also be interpreted as the presence of intact rock, as opposed to ice. Indeed, when the porosity of the subsurface is unknown, the petrophysical joint inversion scheme does not easily differentiate between ice and rock content (Wagner et al., 2019). In order to gain information about porosity, we unsuccessfully attempted to drill a core sample, but due to the quantity of rock at the site, the drill broke at very shallow depths. Nevertheless, for both interpretation outcomes we infer that within this rock glacier, it is likely that the ice has melted, leaving behind large voids filled with air (top layer) or water (deeper layer). We classify El Jote as a relict rock glacier given that it contains little to no ice according to the geophysical results. For both the inversion results it seems that the bedrock is deeper than 100 m for almost the entire profile length, but the strong increase in velocity and resistivity (Fig. 4c and d) and rock content (Fig. 5f) at approximately 60 m depth and at profile lengths of 150 m to 250 m and at approximately 550 m may be interpreted as the top of the bedrock. In addition, the lenses of lower resistivity values ($\rho \sim 10^3\ \Omega\,\mathrm{m}$) and the high water content in the bottom layer (more than 20 %) suggests the presence of an aquifer between the bedrock and the surface of the relict rock glacier.

### 5.3 El Ternero (intact rock glacier)

The inversion model results for El Ternero are slightly shallower than those obtained on El Jote. This is due to the extremely irregular surface of this rock glacier and large voids between boulders, which increased the dispersion of seismic energy and especially due to the failure of one of the two geophone cables: the off-line shots used to link the displaced arrays were recorded only by few of the closest geophones to the shot position, thereby losing ray coverage with depth. Nevertheless, we were able to retrieve useful information from the field measurements. The inversion outcomes show a 5 m-thick active layer made of unconsolidated rock with air-filled pore space, overlaying a ice rich layer (Fig. 7d). Also, the steep increases in velocity values located between 10 m and 25 m depth (Fig. 6d), most likely indicate rock compaction. Nevertheless this layer is not continuous as there are low resistivity anomalies near 150 m and 550 m along the profile line, which correspond to an increase in the water content (up to 17 % in Fig. 7c) which could be a sign of local melting due to permafrost degradation or of reaching bedrock (and the bottom of the ice-rich layer).

### 5.4 Towards a diagnostic model representation for the ice presence in rock glaciers

The results from the petrophysical joint inversion help quantify the volume content of air, water, ice and rock and identify El Jote as relict and El Ternero as intact rock glaciers. However, in many cases such an interpretation is limited by the lack of proper petrophysical models (or parameters). When petrophysical model coupling is not possible, the comparison of velocity and resistivity model inversion results can still deliver plenty of information about the rock-glacier's internal structure. In Fig. 8 we show resistivity-velocity density plots for each rock glacier, built from the individual model inversion results of figures

4(c),(d) and 6(c),(d). The differences between the two rock glaciers are clearly noticeable, with relatively low resistivity and low velocity clusters for the relict rock glacier, while the intact one is associated with higher velocities and resistivities.

The relatively low resistivities and low velocities (Fig. 8a) are in agreement with air filled unconsolidated sediments inferred through the petrophysical joint inversion results (Figs. 5e,f). The lowest resistivities may be associated with liquid water and/or a proglacial aquifer (Fig. 5c; section 5.2).

The gradual increase in resistivity and velocity (Fig. 8b) are evidence of material consolidation such as bedrock or ice-rich layers. Given the very high resistivities (over $10^5\ \Omega\ \mathrm{m}$) our interpretation is that these are ice rich layers (Table 1, resistivity values), which agrees with the petrophysical joint inversion results (Fig. 7d).

The rather different appearance of the two density plots (Fig. 8a and b) can be used as an indicator of the distinct nature of the two rock glaciers: overall, the stagnant rock glacier is characterized by lower resistivities and velocities while the intact rock glacier is indicated by higher resistivity and velocity values, reflecting the ice rich layer. The schematic plot (Fig. 8c) summarizes the findings for our two end-member rock glaciers and could be useful for identifying ice-rich landforms using seismic and electrical resistivity methods.

### 5.5 Hydrogeological role

El Ternero and El Jote represent two end-members of rock glacier types. El Ternero is an intact and likely active rock glacier containing significant amounts of ice according to our geophysical analysis, while El Jote is likely a relict rock glacier whose ice has largely if not completely melted. Each have a distinct and important hydrological role. El Ternero has the capacity to function as long-term water storage given that most of the water it contains is in the form of ice which is insulated from the environment by debris cover ($\sim$ 5 m thick). The insulating effect of the debris cover has been shown to slow the rate of melt (Jones et al., 2018; Bonnaventure and Lamoureux, 2013) making rock glaciers more resilient to climate change compared to debris-free glaciers.

El Jote likely has an important hydrological role as an aquifer and in terms of its influence on water flow. The petrophysical results suggest that it contains an aquifer which may play a role in storing and delaying the release of water downstream, assuming its hydrological role is similar to that of the relict rock glacier Schöneben in the Austrian Alps (Winkler et al., 2016).

## 6 Conclusion and Outlook

In this study, we presented the first comparison of geophysical signatures of one intact and one stagnant rock glacier using refraction seismic and electrical resistivity tomography inversion results in the Chilean Andes. The obtained tomograms present much higher velocities and resistivities for the intact rock glacier, which we interpreted as a much higher ice content accordingly to physical parameters for ERT and RST surveys on rock glaciers (Table 1) and to the petrophysical inversion model results.

The resistivity-velocity density plots show a clear signature difference for these rock glaciers, which makes sense given that El Jote is classified as a relict rock glacier with an aquifer below and El Ternero is an intact (active) rock glacier.

Through the joint interpretation of ERT and RST surveys for El Jote we were able to detect the top of the bedrock in part of the model domain and identify a potential aquifer, while in case of El Ternero the active layer and the top of an ice-rich layer were identified, together with signs of its partial melting at the bottom of the investigated area. The geophysical results confirm that El Ternero is an intact rock glacier with a significant amount of ice and that El Jote contains little to no ice (relict rock glacier).

There is ambiguity in the interpretation between the presence of ice or a rock matrix where resistivities are relatively high, especially for El Jote inversion results. This could be improved adding information about subsurface porosity or by the incorporation of additional freeze–thaw sensitive data sets such as complex electrical resistivity measurements (Wagner et al., 2019). In addition, to increase the investigated depth it would be necessary to improve the seismic data quality, which could be done by fastening the geophones to the surface by drilling small holes in the rock, although this would be logistically complicated.

## Appendix A: Petrophysical joint inversion

Petrophysical coupling allows the inversion of separate data sets to determine common parameters through petrophysical relationships. Within this framework, Wagner et al. (2019) developed an inversion scheme which allows the interpretation of seismic refraction traveltimes and apparent resistivities in terms of ice, water, air and rock content. The inversion is based on a petrophysics four phase model (4PM; Hauck et al., 2011), where partly or permanently frozen subsurface systems are assumed to be comprised of the volumetric fractions of the solid rock matrix ($\mathrm{f_r}$) and a pore-filling mixture of liquid water ($\mathrm{f_w}$), ice ($\mathrm{f_i}$) and air ($\mathrm{f_a}$):

$$\mathrm{f_r} + \mathrm{f_w} + \mathrm{f_i} + \mathrm{f_a} = 1. \tag{A1}$$

The treatment of the rock volumetric fraction as a single phase is a justified simplification in rock glacier environment, where the amount of soil is negligible compared to the hard rock.

The volumetric fractions in Eq. (A1) are related to the seismic slowness (s), reciprocal of the P-wave propagation velocity (v), through the time averaging equation (Timur, 1968):

$$\mathrm{s} = \frac{1}{\mathrm{v}} = \frac{\mathrm{f_r}}{\mathrm{v_r}} + \frac{\mathrm{f_w}}{\mathrm{v_w}} + \frac{\mathrm{f_i}}{\mathrm{v_i}} + \frac{\mathrm{f_a}}{\mathrm{v_a}}, \tag{A2}$$

and to the electrical resistivity through a modification of Archie's second law (Archie, 1942):

$$\rho = \rho_\mathrm{w}(1-\mathrm{f_r})^{-\mathrm{m}} \left(\frac{\mathrm{f_w}}{1-\mathrm{f_r}}\right)^{-\mathrm{n}}, \tag{A3}$$

where the porosity is expressed in terms of rock content ($\phi = 1 - \mathrm{f_r}$). The assumptions within this 4PM model are that the medium is isotropic, at high effective pressure and has a single homogeneous mineralogy (validity of Eq. A2), and that the electric current flow is dominated by electrolyte conduction (validity of Eq. A3).

The petrophysical joint inversion scheme minimizes the following objective function (Wagner et al., 2019; Mollaret et al., 2020):

$$\Phi = \Phi_\mathrm{d} + \lambda\Phi_\mathrm{m} + \lambda_\mathrm{p}\Phi_\mathrm{p}. \tag{A4}$$

$\Phi_d$ refers to the combined data misfit, while $\Phi_m$ represents a smoothness regularization term build through four first-order roughness operators to promote smoothness in the distribution of each constituent of the four-phase system. The last term is an additional regularization term which constraints the volume conservation (Eq. A1). The two weights $\lambda$ and $\lambda_p$ are responsible for scaling the influences of the two regularization terms, where $\lambda$ is chosen to fit the data within the error bound and $\lambda_p$ is chosen large enough to prohibit non-physical solutions.

Within this framework, the RST and ERT observations are used to infer the volumetric fractions of water, ice, air and rock for each model cell, while the spatial distribution of electrical resistivity and P-waves velocities are obtained through Eq. (A2) and Eq. (A3), where the petrophysical parameters and constituent velocities are assumed to be spatially constant. We chose the values for the inversion of the field observations based on the literature (Hauck and Kneisel, 2008; Maurer and Hauck, 2007; Hauck et al., 2011; Wagner et al., 2019) which are listed in Table A1. Such parameters are of value in periglacial environments and consistent with the relevant physical parameters for ERT and RST value also presented in Table 1, nevertheless geotechnical in situ measurements could improve the estimation of those and therefore the accuracy of the inversion model results. A last important parameter to consider in this scheme is porosity initial value and range. Wagner et al. (2019), already stressed the importance of a good porosity estimation in order to avoid ambiguity between ice and rock content and in a recent study, Mollaret et al. (2020) analyses the influence of the porosity constraint in the petrophysical joint inversion results. Following the approach of this last paper, and accordingly to the previous knowledge from the field site we tested different initial porosity values and ranges ($\phi_{min}$-$\phi_{max}$) for both rock glaciers. The choice was made selecting the less constraining intervals which allowed results consistent with the hypothesis of rock glacier formations and the surface geology of the two sites.

## A1 Inversion parameters for El Jote and El Ternero rock glaciers.

For both field locations we applied the same regularization weight, as for the individual inversion: $\lambda = 10$, while for ensuring the volume conservation we applied $\lambda_p = 10000$. Regularization weights were chosen as illustrated by Mollaret et al. (2020), considering both, classic L-curve analysis and the sum of the components fractions. For El Jote the initial porosity was set to an homogeneous 30 % and inverted for in a range going from 0 % to 80 %, heterogeneously within the model. While for El Ternero the initial porosity was set to an homogeneous 60 % and inverted within a range going from 10 % to 90 %, heterogeneously within the model. These values were tested as mentioned in the previous section with a maximum variation within the average volume contents of the inversion model results of 5%. After 15 iterations we obtained an overall data fit corresponding to $\chi^2 = 1.45$ and $\chi^2 = 1.65$ for El Jote and El Ternero, respectively.

*Acknowledgements.* The field campaign to obtain the geophysical profiles on the two glaciers was logistically and physically challenging because of the location and altitude. This data collection was possible thanks to: Eduardo Yáñez San Francisco, Gonzalo Navarro Chamal, Marcelo Marambio Portilla, Ivan Fuentes, Jorge Sanhueza Soto, Benjamin Lehmann, Ayón García Piña, Christopher Ulloa Correa and Ignacio Díaz Navarro. We also wish to thank Claudio Jordi for sharing his code and Florian Wagner and his research group for making it available to the public. We thank Ignacio Castro Cancino for his contribution to the rock glacier descriptions and for providing the MAAT data for the station in Estero Derecho. This work was supported by CONICYT-Programa Regional-Fortalecimiento (R16A10003) and FIC-R (2016) Coquimbo (BIP: 40000343). Nicole Schaffer was supported by ANID-FONDECYT-Postdoctorado (3180417). Also, we would like to thanks the editor and the reviewers who helped clarify and re-structure the paper through the review process.

*Author contributions.* GdP and RV analysed the data. GdP ran the inversions and wrote most of the manuscript except Sections 2 and 5.5, which were written by NS. RV, SM and NS designed the study, organised the field campaign, reviewed and edited the manuscript. All authors contributed to the study.

*Competing interests.* No competing interest are present.

## References


Aguilar, G., Riquelme, R., Martinod, J., and Darrozes, J.: Rol del clima y la tectónica en la evolución geomorfológica de los andes semiáridos chilenos entre los 27-32°S., Andean Geology, 40, 79–101, 2013.

Archie, G.: The electrical resistivity log as an aid in determining some reservoir characteristics., Trans. AIME, 146, 54–62, 1942.

Azòcar, G. and Brenning, A.: Hydrological and geomorphological significance of rock glaciers in the dry Andes, Chile (27°–33°S)., Permafrost Periglacial Processes, 21, 42–53, 2010.

Ballantyne, C.: Periglacial geomorphology., Quaternary Science Reviews, 21, 1935–2017, 2002.

Banerjee, B. and Gupta, S.: Hidden layer problem in seismic refraction work., Geophysical Prospecting, 23, 542–652, 1975.

Barcaza, G., Nussbaumer, S. U., Tapia, G., Valdés, J., García, J.-L., Videla, Y., Albornoz, A., and Arias, V.: Glacier inventory and recent glacier variations in the Andes of Chile, South America, Annals of Glaciology, 58, 166–180, https://doi.org/10.1017/aog.2017.28, 2017.

Barsch, D.: Rock glaciers and ice-cored moraines., Geografiska Annaler, 53, 203–206, 1971.

Barsch, D.: Origin and geoelectrical resistivity of rock glaciers in semiarid subtropical mountains (Andes of Mendoza, Argentina)., Geomorphology, 33, 151–163, 1989.

Barsch, D.: Permafrost creep and rockglaciers, Permafrost and Periglacial Processes, 3, 175–188, https://doi.org/https://doi.org/10.1002/ppp.3430030303, https://onlinelibrary.wiley.com/doi/abs/10.1002/ppp.3430030303, 1992.

Barsch, D.: Rockglaciers., Springer-Verlag, Berlin, 1st edn., 1996.

Berthling, I.: Beyond confusion: rock glaciers as cryo-conditioned landforms., Geomorphology, 131, 98–106, 2011.

Binley, A. and Kemna, A.: Hydrogeophysics. Water Science and Technology Library., vol. 50, chap. DC Resistivity and Induced Polarization Methods., Springer Netherlands, Dodrecht, 2005.

Bodin, X., Rojas, F., and Brenning, A.: Status and evolution of the cryosphere in the Andes of Santiago (Chile, 33.5°S)., Geomorphology, 118, 453–464, 2010.

Bonnaventure, P. and Lamoureux, S.: The active layer: A conceptual review of monitoring, modelling techniques and changes in a warming climate., Progress in Physical Geography, 37, 352–376, 2013.

Brenning, A., Grasser, M., and Friend, D.: Statistical estimation and generalized additive modeling of rock glacier distribution in the San Juan Mountains, Colorado, United States., Journal of Geophysical Research: Earth Surface, 112, F02S15, 2007.

Cogley, J., Hock, R., Rasmussen, L., Arendt, A., Bauder, A., and Braithwaite, R.: Glossary of glacier mass balance and related terms, Paris: IHP-VII technical documents in hydrology no. 86, IACS contributionno. 2, UNESCO-IHP, 2011.

Colucci, R., Forte, E., Zebre, M., Maset, E., Zanettini, C., and Guglielmin, M.: Is that a relict rock glacier?, Geomorphology, 330, 177–189, 2019.

Croce, F. and Milana, J.: Internal structure and behaviour of a rock glacier in the arid Andes of Argentina., Permafrost and Periglacial Processes, 13, 289–299, 2002.

Dahlin, T.: 2D resistivity surveying for environmental and engineering applications., First Break, 14, 275–283, 1996.

Daily, W., Ramirez, A., LaBrecque, D., and Nitao, J.: Electrical resistivity tomography of vadose water movement., Water Resources Research, 28, 1429–1442, 1992.

de Lima, A.: Water saturation and permeability from resistivity, dielectric, and porosity logs., Geophysics, 60, 1756–1764, 1995.

Delaloye, R. and T, T. E.: IPA Action Group Rock glacier inventories and kinematics: Towards standard guidelines for inventorying rock glaciers. Baseline concepts v 4.1., retrieved from http://https://www3.unifr.ch/geo/geomorphology/en/research/ipa-action-group-rock-glacier/ (Accessed 20Jan 2020)., 2020.

DGA.: Atlas del Agua, Chile, retrieved from: https://dga.mop.gob.cl/atlasdelagua/Paginas/default.aspx (Accessed 1 Nov 2017)., 2016.

Draebing, D. and Krautblatter, M.: P-wave velocity changes in freezing hard low-porosity rocks: a laboratory based time-average model., The Cryosphere, 6, 1163–1174, 2012.

Duvillard, P. A., Revil, A., Qi, Y., Soueid Ahmed, A., Coperey, A., and Ravanel, L.: Three-Dimensional Electrical Conductivity and Induced Polarization Tomography of a Rock Glacier, Journal of Geophysical Research: Solid Earth, 123, 9528–9554, https://doi.org/https://doi.org/10.1029/2018JB015965, https://agupubs.onlinelibrary.wiley.com/doi/abs/10.1029/2018JB015965, 2018.

Evin, M., Fabre, D., and Johnson, P.: Electrical resistivity measurements on the rock glaciers of Grizzly Creek, St Elias Mountains, Yukon., Permafrost and Periglacial Processes, 8, 181–191, 1997.

Favier, V., Falvey, M., Rabatel, A., Praderio, E., and López, D.: Interpreting discrepancies between discharge and precipitation in high-altitude area of Chile's nortechico region (26–32°S)., water Resources Research, 45, 1–20, 2009.

Garreaud, R.: The Andes climate and weather., Advances in Geosciences, 22, 3–11, 2009.

Gascoin, S., Kinnard, C., Ponce, R., Lhermitte, S., Macdonell, S., and Rabatel, A.: Glacier contribution to streamflow in two headwaters of the Huasco River, Dry Andes of Chile, The Cryosphere, 5, 1099–1113, https://doi.org/10.5194/tc-5-1099-2011, 2011.

Günther, T., Rücker, C., and Spitzer, K.: Three-dimensional modeling and inversion of DC resistivity data incorporating topography–II. Inversion., Geophysics Journal International, 166, 506–517, 2006.

Halla, C., Blöthe, J., Baldis, C., Trombotto, D., Hauck, C., and Schrott, L.: Ice content and interannual water storage changes of an active rock glacier in the dry Andes of Argentina., The Cryosphere., https://doi.org/https://doi.org/10.5194/tc-2020-29, 2020.

Hansen, P.: The L-Curve and Its Use in the Numerical Treatment of Inverse Problems, Computational Inverse Problems in Electrocardiology, 4, 119–142, 2001.

Harrington, J., Mozil, A., Hayashi, M., and Bentley, L.: Groundwater flow and storage processes in an inactive rock glacier, Hydrological Processes, 32, 3070–3088, 2018.

Hauck, C. and Kneisel, C.: Applied Geophysics in Periglacial Environments., Cambridge University Press, Cambridge, 1st edn., 2008.

Hauck, C., Mühll, D. V., and Maurer, H.: DC resistivity tomography to detect and characterize mountain permafrost., Geophysical Prospecting, 51, 273–284, 2003.

Hauck, C., Isaksen, K., Mühll, D. V., and Sollid, J.: Geophysical surveys designed to delineate the altitudinal limit of mountain permafrost: an example from Jotunheimen, Norway., Permafrost and Periglacial Processes, 15, 191–205, 2004.

Hauck, C., Böttcher, M., and Maurer, H.: A new model for estimating subsurface ice content based on combined electrical and seismic data sets., Cryosphere, 5, 453–468, 2011.

Hausmann, H., Grainer, K., Brückl, E., and Mostler, W.: Internal Structure and Ice Content of Reichenkar Rock Glacier (Stubai Alps, Austria) Assessed by Geophysical Investigations., Permafrost and Periglaclacial Processes, 28, 351–367, 2007.

Hock, R., Rasul, G., Adler, C., Cáceres, B., Gruber, S., Hirabayashi, Y., Jackson, M., Kääb, A., Kang, S., Kutuzov, S., Milner, A., Molau, U., Morin, S., Orlove, B., and Steltzer, H.: Special Report on the Ocean and Cryosphere in a Changing Climate [H.-O. Pörtner, D.C. Roberts, V. Masson-Delmotte, P. Zhai, M. Tignor, E. Poloczanska, K. Mintenbeck, A. Alegría, M. Nicolai, A. Okem, J. Petzold, B. Rama, N.M. Weyer (eds.)], chap. High Mountain Areas, The Intergovernmental Panel on Climate Change (IPCC), 2019.

Jones, D., Harrison, S., Anderson, K., and Betts, R.: Mountain rock glaciers contain globally significant water stores., Scientific Reports, 8, 2018.

Krainer, K. and Mostler, W.: Flow velocities of active rock glaciersin the Austrian Alps., Geografiska Annaler, 88, 267–280, 2006.

Langston, G., Bentley, L., Hayashi, M., McClymont, A., and Pidlisecky, A.: Internal structure and hydrological functions of an alpine proglacial moraine., Hydrological processes, 25, 2967–2982, 2011.

Lesmes, D. and Friedman, S.: Hydrogeophysics. Water Science and Technology Library., vol. 50, chap. Relationships between the Electrical and Hydrogeological Properties of Rocks and Soils., Springer Netherlands, Dodrecht, 2005.

Maurer, H. and Hauck, C.: Instruments and Methods: Geophysical imaging of alpine rock glaciers., Journal of Glaciology, 53, 110–120, 2007.

Mollaret, C., Wagner, F., Hilbich, C., Scapozza, C., and Hauck, C.: Petrophysical Joint Inversion Applied to Alpine Permafrost Field Sites to Image Subsurface Ice, Water, Air, and Rock Contents, Frontiers in Earth Science, 8, 85, 2020.

Monnier, S. and Kinnard, C.: Internal structure and composition of a rock glacier in the Dry Andes, inferred from ground-penetrating radar data and its artefacts., Permafrost Periglacial Processes, 26, 335–346, 2015.

Nolet, G.: Seismic Tomography. Seismology and Exploration Geophysics., vol. 5, chap. Seismic wave propagation and seismic tomography., Springer Netherlands, Dodrecht, 1987.

Núñez, J., Rivera, D., Oyarzùn, R., and Arumí, J.: Influence of Pacific Ocean multi decadal variability on the distributional properties of hydrological variables in north-central Chile., Journal of Hydrology, 501, 227–240, 2013.

Oyarzùn, J. and Oyarzùn, R.: Sustainable development threats, inter-sector conflicts and environmental policy requirements in the arid, mining rich, northern Chile territory., Sustainable Development, 19, 263–274, 2011.

Potter, N.: Ice-Cored Rock Glacier, Galena Creek, Northern Absaroka Mountains, Wyoming., Geological Society of America Bulletin, 83, 3025–3058, 1972.

Pourrier, J., Jourde, H., Kinnard, C., Gascoin, S., and Monnier, S.: Glacier meltwater flow paths and storage in a geomorphologically complex glacial foreland: The case of the Tapado glacier, dry Andes of Chile., Journal of Hydrology, 519, 1068–1083, 2014.

Revil, A. and Glover, P.: Theory of ionic-surface electrical conduction in porous media., Physical Review B, 55, 1757–1773, 1997.

Rücker, C., Günther, T., and Wagner, F.: pyGIMLi: An open-source library for modelling and inversion in geophysics., Computers and Geosciences, 109, 106–123, 2017.

Réveillet, M., MacDonnel, S., Gascoin, S., Kinnard, C., Lhermitte, S., and Schaffer, N.: Impact of forcing on sublimation simulations for a high mountain catchment in the semiarid Andes., The Cryosphere, 14, 147–163, 2020.

Schaffer, N., MacDonell, S., Réveillet, M., Yáñez, E., and Valois, R.: Rock glaciers as a water resource in a changing climate in the semiarid Chilean Andes., Regional Environmental Change, 19, 1263–1279, 2019.

Schrott, L.: Some geomorphological-hydrological aspects of rock glaciers in the Andes (San Juan, Argentina)., Zeitschrift fur Geomorphologie, Supplementband, 104, 161–173, 1996.

Sinclair, K. and MacDonell, S.: Seasonal evolution of penitente glaciochemistry at Tapado Glacier, Northern Chile., Hydrological Processes, 30, 176–186, 2016.

Thies, H., Nickus, U., Mair, V., Tessadri, R., Tait, D., Thaler, B., and Psenner, R.: Unexpected response of high alpine lake waters to climate warming., Environmental Science and Technology, 41, 7424–7429, 2007.

Timur, A.: Velocity of compressional waves in porous media at permafrost temperatures., Geophysics, 33, 584–595, 1968.

Valois, R., Galibert, P., Guérin, R., and Plagnes, V.: Application of combined time-lapse seismic refraction and electrical resistivity tomography to the analysis of infiltration and dissolution processes in the epikarst of the Causse du Larzac (France)., Near Surface Geophysics, 14, 13–22, 2016.

Valois, R., Cousquer, Y., Schmutz, M., Pryet, A., Delbart, C., and Dupuy, A.: Characterizing Stream-Aquifer Exchanges with Self-Potential Measurements., Hydrogeology Journal, 56, 437–450, 2018a.

Valois, R., Vouillamoz, J., Lun, S., and Arnout, L.: Mapping groundwater reserves in northwestern Cambodia with the combined use of data from lithologs and time-domain-electromagnetic and magnetic-resonance soundings., Hydrogeology Journal, 26, 1187–1200, 2018b.

Valois, R., MacDonell, S., Núñez-Cobo, J., and Maureira-Cortés, H.: Groundwater level trends and recharge event characterization using historical observed data in semi-arid Chile., Hydrological Sciences Journal, 65, 597–609, 2020a.

Valois, R., Schaffer, N., Figueroa, R., Maldonato, A., Yáñez, E., Hevia, A., Carrizo, G. Y., and MacDonell, S.: Characterizing the Water Storage Capacity and Hydrological Role of Mountain Peatlands in the Arid Andes of North-Central Chile., Water, 12, 1071, 2020b.

Vonder-Mühll, D., Hauck, D., and Gubler, C.: Mapping of mountain permafrost using geophysical methods., Progress in Physical Geography, 26, 643–660, 2002.

Wagner, F., Mollaret, C., Günther, T., Kemna, A., and Hauck, C.: Quantitative imaging of water, ice and air in permafrost systems through petrophysical joint inversion of seismic refraction and electrical resistivity data., Geophysics Journal International, 219, 1866–1875, 2019.

White, D.: Two-Dimensional Seismic Refraction Tomography., Geophysics Journal International, 97, 223–245, 1989.

Winkler, G., Wagner, T., M. Pauritsch, S. B., Kellerer-Pirklbauer, A., Benischke, R., Leis, A., Morawetz, R., Schreilechner, M. G., and Hergarten, S.: Identification and assessment of groundwater flow and storage components of the relict Schöneben Rock Glacier, Niedere Tauern Range, Eastern Alps (Austria)., Hydrogeology Journal, 24, 937–953, 2016.

Yáñez, G., Renero, C., von Huene, R., and Díaz, J.: Magnetic anomaly interpretation across the southern-central Andes (32-34S): The role of the Juan Fernández Ridge in the late Tertiary evolution of the margin., Journal of Geophysical Research: Solid Earth, 106, 6325–6345, 2001.

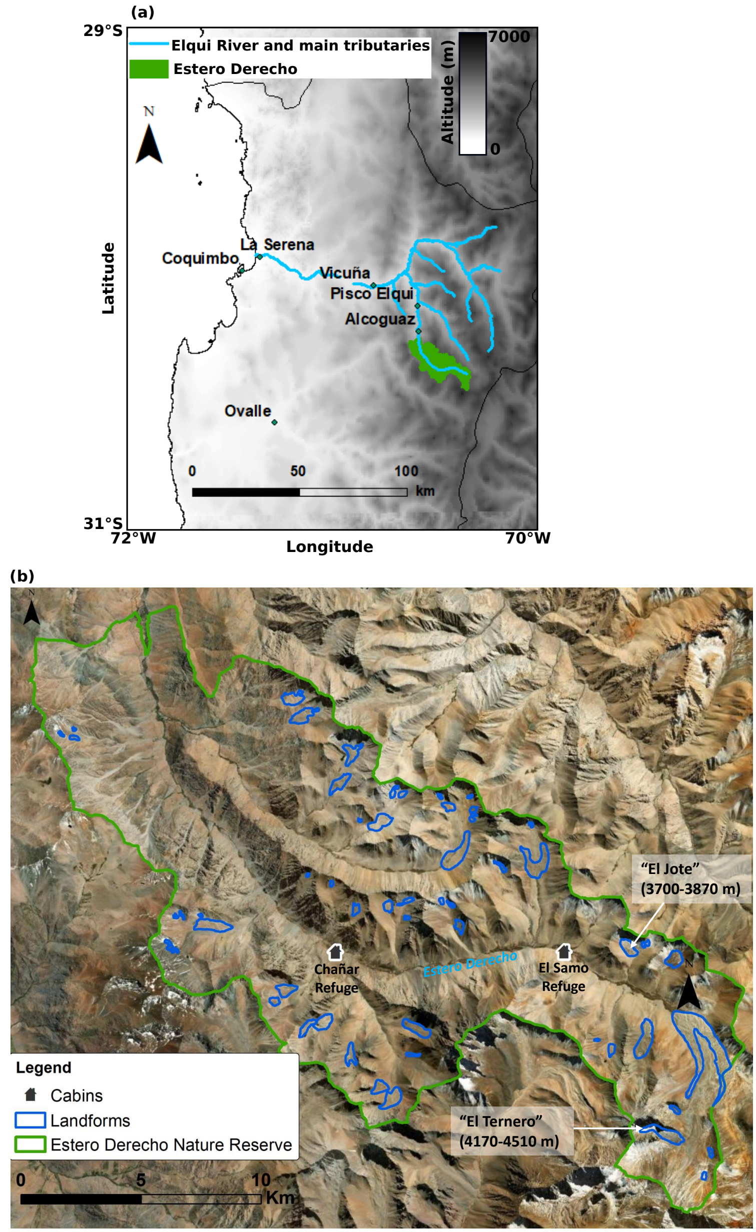


**Figure 1.** (a) Overview map indicating the location of Estero Derecho ($\sim$ 30°S, 70°W) in the Coquimbo Region of Chile. Elevation map from ASTER GDEM. (b) Detailed map of Estero Derecho with an inventory of landforms created by CEAZA. The delineations for El Jote and El Ternero were created specifically for this study from the Esri base-map satellite imagery. Both landforms are labeled with their respective elevation ranges.

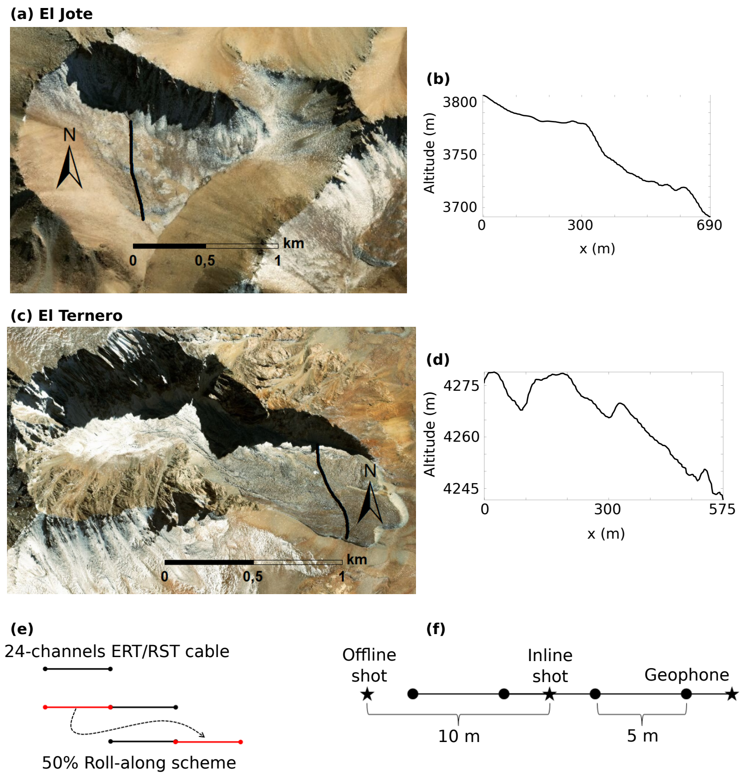


**Figure 2.** (a) Aerial image of El Jote, showing the location of the geophysical survey line and (b) its topography from field differential GPS measurements. (c) Aerial image of El Ternero, showing the location of the geophysical survey line and (d) its topography from field differential GPS measurements. Base maps in (a) and (c) from Esri World Imagery 2018. (e) Scheme of the 50 % roll-along scheme used for ERT surveys on both rock glaciers and RST survey on El Jote. (f) Scheme of geophones and Inline/Offline shot positions for RST surveys.

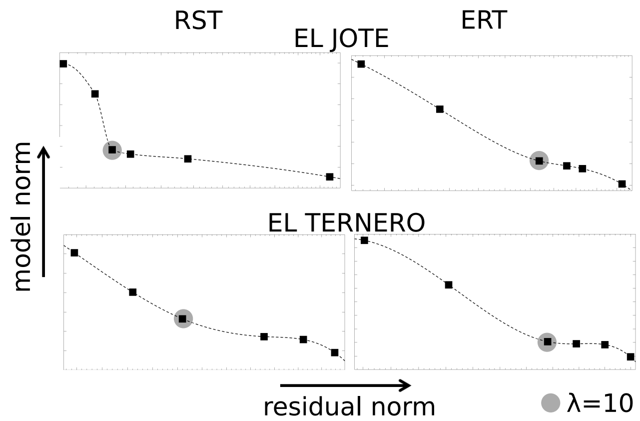


**Figure 3.** L-curve analysis for the regularization weights ($\lambda$) used in the inversion of ERT and RST data on both rock glaciers. In each plot, the values tested are $\lambda$= 1, 5, 10, 15, 50, 100.

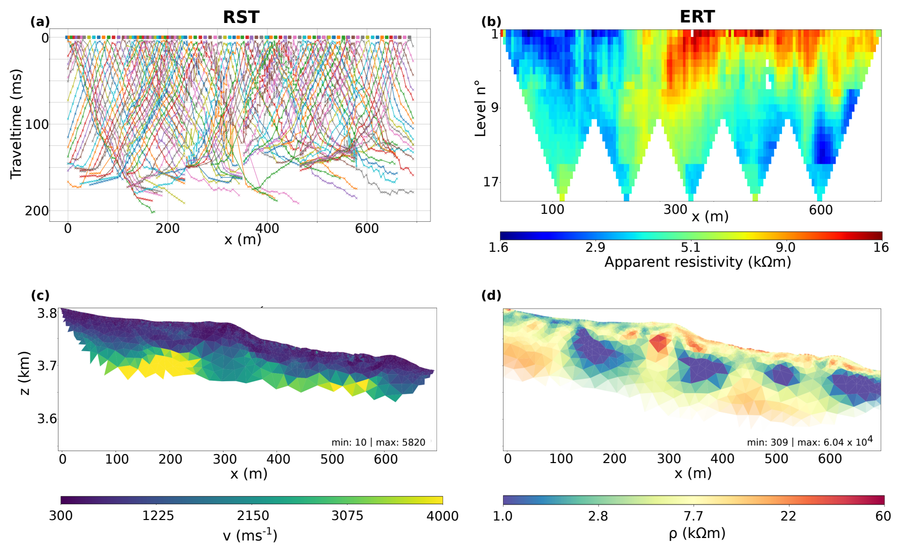


**Figure 4.** Geophysical observations and inversion model results for El Jote rock glacier. (a) RST first arrival traveltimes. (b) ERT apparent resistivity. (c) Velocity and (d) resistivity tomograms. The velocity model is cut below the lowermost ray-path while the resistivity model transparency is proportional to the ERT data coverage. The velocity colorbar is linear, while the resistivity one is expressed in logarithmic scale.

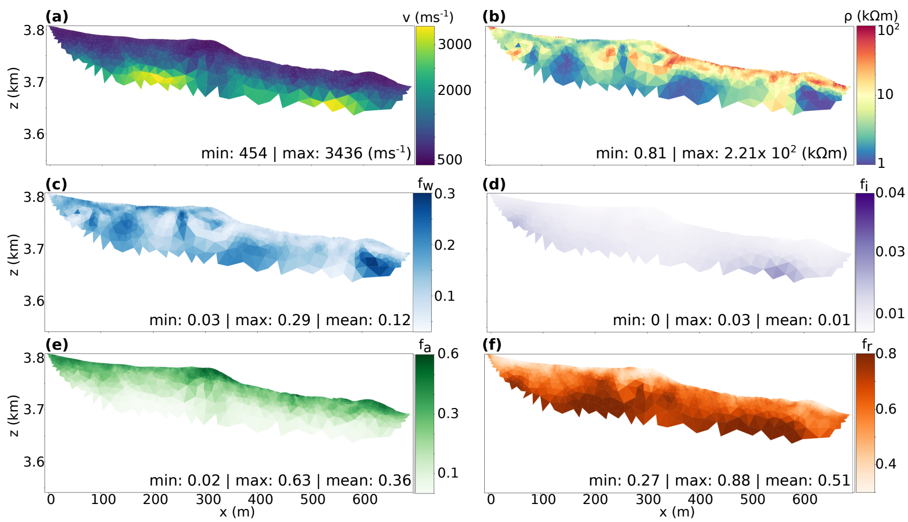


**Figure 5.** Petrophysical joint inversion results of El Jote field data sets. The tomograms represents (a) velocity and (b) resistivity transformed models. The directly inverted parameters are (c) water, (d) ice, (e) air and (f) rock volumetric content. All models are cut off below the lowermost ray path, with only resistivity colorbar expressed in logarithmic scale.

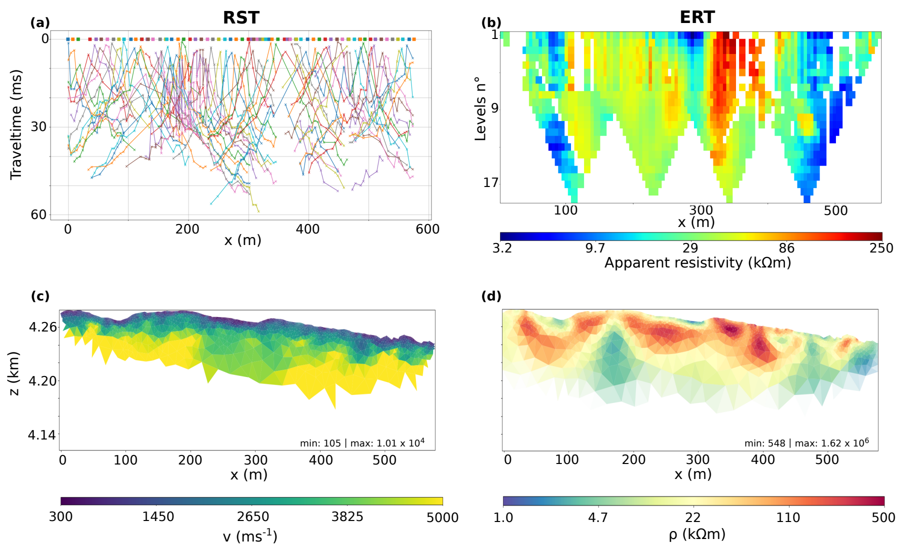


**Figure 6.** Geophysical observations and inversion model results for El Ternero rock glacier. (a) RST first arrival traveltimes. (b) ERT apparent resistivity. (c) Velocity and (d) resistivity tomograms. The velocity model is cut below the lowermost ray-path while the resistivity model transparency is proportional to the ERT data coverage. The velocity colorbar is linear, while the resistivity one is expressed in logarithmic scale.

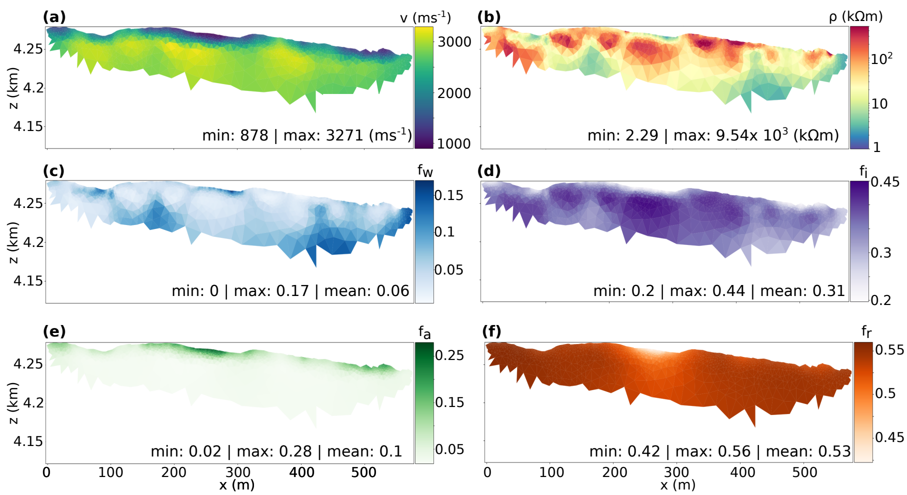


**Figure 7.** Petrophysical joint inversion results of El Ternero field data sets. The tomograms represents (a) velocity and (b) resistivity transformed models. The directly inverted parameters are (c) water, (d) ice, (e) air and (f) rock volumetric content. All models are cut off below the lowermost ray path, with only resistivity colorbar expressed in logarithmic scale.

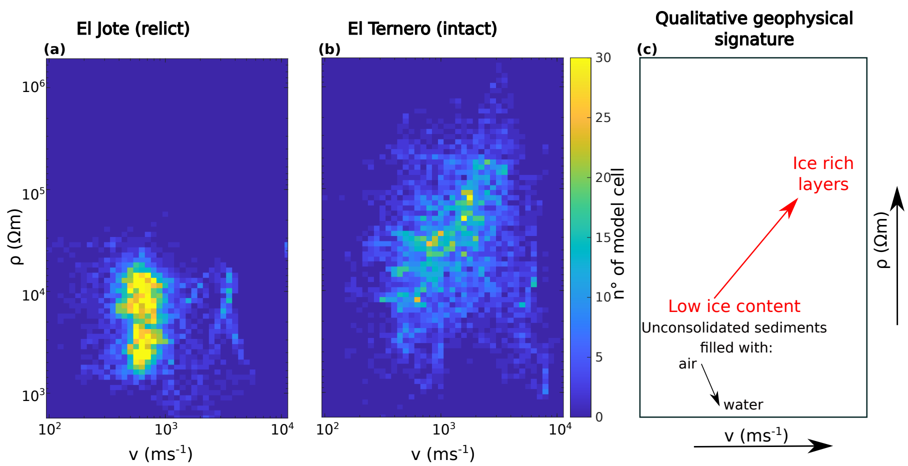


**Figure 8.** Density plots of resistivity versus P-waves velocity values for (a) El Jote and (b) El Ternero datasets. (c) Schematic plot of the qualitative ERT and RST signature for intact and stagnant rock glaciers.

**Table 1.** Relevant physical parameters for ERT and RST surveys on rock glaciers (table compiled from Hauck and Kneisel, 2008 and Maurer and Hauck, 2007).

| | Electrical resistivity ($\Omega$ m) | P-wave velocity (m $s^{-1}$) |
|---|---|---|
| Sand-Gravel | $10^2 - 10^4$ | 400-2500 |
| Rock | $10^3 - 10^5$ | 3000-6500 |
| Glacial ice | $10^6 - 10^8$ | 3100-4500 |
| Frozen sediments, ground ice, permafrost | $10^3 - 10^6$ | 2500-4300 |
| Water | $10^1 - 10^2$ | 1500 |
| Air | $10^{14}$ | 330 |

**Table 2.** Acquisition settings for ERT and RST profiles on El Ternero and El Jote.

| | El Jote | | El Ternero | |
|---|---|---|---|---|
| | ERT | RST | ERT | RST |
| sensor positions | 144 | 144 | 120 | 120 |
| sensors spacing (m) | 5 | 5 | 5 | 5 |
| number of shots | - | 98 | - | 75 |
| shots spacing (m) | - | 10 | - | 10 |
| profile length (m) | 690 | 690 | 575 | 575 |
| data points | 2135 | 4575 | 1479 | 1400 |
| measurement errors | 1.2 % | 0.001 (s) | 11.4 % | 0.001 (s) |

**Table A1.** Parameters used for the petrophysical joint inversion of El Jote and El Ternero datasets (eqs.A2 and A3).

| Archie parameters | | Constituent velocities | |
|---|---|---|---|
| $\rho_\mathrm{w}$ | $60\ (\Omega\ \mathrm{m})$ | $\mathrm{v_w}$ | $1500\ (\mathrm{m\,s^{-1}})$ |
| n | 2.4 | $\mathrm{v_i}$ | $3500\ (\mathrm{m\,s^{-1}})$ |
| m | 1.4 | $\mathrm{v_a}$ | $330\ (\mathrm{m\,s^{-1}})$ |
| | | $\mathrm{v_r}$ | $6000\ (\mathrm{m\,s^{-1}})$ |